Phase differences of near-threshold high-order harmonics generated in atoms and molecules

Kosaku Kato,* Shinichirou Minemoto, Yusuke Sakemi, and Hirofumi Sakai†
Department of Physics, Graduate School of Science, The University of Tokyo, 7-3-1 Hongo, Bunkyo-ku, Tokyo 113-0033, Japan
(Received 29 October 2014; published 1 December 2014)

We present the observations of the phase differences $\Delta\phi_{\mathrm{HH}}^{(2n)}$ between adjacent high-order harmonics generated from Ar and N_2 at the near-threshold region. The $\Delta\phi_{\mathrm{HH}}^{(2n)}$'s are extracted from the photoelectron signals resulting from two-color two-photon ionization of rare-gas atoms, which are produced by high-order harmonics to be measured and a part of the fundamental pulse for probing. An analysis method is employed to remove the inevitable modulations in high-order-harmonic intensities based on the underlying mechanism of the production of photoelectrons. We find a significant difference in the $\Delta\phi_{\mathrm{HH}}^{(2n)}$ at the nearest-threshold order between Ar and N_2. This difference cannot be reproduced by the model calculation by using the saddle-point method within the strong-field approximation. To elucidate the origin of the difference between the $\Delta\phi_{\mathrm{HH}}^{(2n)}$ for Ar and that for N_2, we note the fact that the phase difference $\Delta\phi_{\mathrm{HH}}^{(2n)}$ contains information both on the recombination time t_r of the freed electron and on the phase of the recombination dipole moment d^*. With the help of some numerical calculations, we discuss the effect of the potential created by the parent ion on t_r and d^* which are neglected in the strong-field approximation.

DOI: 10.1103/PhysRevA.90.063403 PACS number(s): 32.80.Wr, 33.80.Wz, 42.65.Ky

I. INTRODUCTION

High-order harmonics generated from atoms and molecules are regarded as the most promising tool to explore ultrafast phenomena with an unprecedented time resolution. From the viewpoint of a light source, their pulse width reaches the shortest of tens of attoseconds, and from the viewpoint of light-matter interaction, electron and nuclear dynamics can be traced with subfemtosecond, subangstrom resolutions by high-order-harmonic spectra [1–3]. High-order-harmonic generation is understood by the three-step model [4]: (1) An atom or molecule is ionized by an intense laser field and an electron is released from the potential. (2) The released electron is driven and accelerated by the laser field and returned to the parent ion. (3) The returning electron recombines with the parent ion and its kinetic energy is transferred to a high-energy photon. According to this model, high-order harmonics can extend to the energy of $3.17U_p + I_P$ with U_p the ponderomotive energy and I_P the ionization potential.

The high-order harmonics far above I_P are well described by the strong-field approximation [5], where the Coulomb potential of the parent ion can be ignored for the trajectories of the returning electron. This approximation allows us to extract the image of atomic or molecular orbitals from the harmonic spectra [6]. Using a sample of aligned molecules, high-order-harmonic spectra give us valuable information about molecular electronic and geometric structures [6–11]. On the other hand, in the energy region near the ionization potential, the harmonic generation process is strongly influenced by the Coulomb potential of the parent ions and cannot be described within the strong-field approximation. It was reported in 1995 that the 13th harmonic intensity generated in Ne is higher when the driving pulse has a nonzero value of ellipticity than that generated with a linearly polarized pulse [12,13], though under the three-step model assuming the strong-field approximation, the high-order harmonics are expected to be maximized at the linear polarization. Recently, similar phenomena were also found by Soifer *et al.* [14]: They show that the high-order harmonics from aligned O_2 molecules are maximized at a nonzero value of ellipticity of the driving pulse when the harmonic photon energy is near I_P. The phenomena beyond the strong-field approximation attract increasing attention to understand more deeply the underlying mechanism of high-order-harmonic generation in the vicinity of Coulomb potential and to extract the information about atomic or molecular orbitals.

We expect that at the near-threshold region the spectral phase of the high-order harmonics will show different behaviors from those at far-above threshold region. The phase differences between adjacent harmonic orders are closely related to the time when the returning electron recombines with the parent ion [15]. Thus, when the Coulomb potential affects the trajectories of the electron its effect should appear in the phase difference. In addition, at the recombination the electron with low energy undergoes a phase shift depending on the shape of the potential, and this shift will be encoded in the phase of the harmonics [16]. In this paper, we report the observations of the phase differences of high-order harmonics in the near-threshold region generated in Ar and N_2, and discuss the origin of the difference between them. A significant difference found between the near-threshold harmonics of Ar and those of N_2, whose ionization potentials are almost the same, is explained in terms of the electron trajectories and the phase shift of the electron de Broglie wave. This paper is organized as follows: In Sec. II, we briefly review the theoretical background of the harmonic phase and explain the principle of its detection. Next, Sec. III presents the details of our experimental setup. In Sec. IV, we present the experimental results and the analysis of them and in Sec. V we discuss the origins of our findings. Finally we summarize the results in

*Present address: Institute of Laser Engineering, Osaka University, 2-6 Yamadaoka, Suita, Osaka 565-0871, Japan.
†hsakai@phys.s.u-tokyo.ac.jp

Sec. VI. Throughout this paper the atomic units and the length gauge are used unless otherwise stated.

II. THEORETICAL BACKGROUND

In this section, the theories about the phase of high-order harmonics are reviewed. In Sec. II A, we explain the relation among the phase differences between adjacent high-order harmonics, the moment when the harmonics are emitted, and the phase of the recombination dipole moment. In Sec. II B we explain the method we used for the detection of the phase difference.

A. Relation between the phase differences and the characteristic times in the process of high-order-harmonic generation

As pointed out in the work by Mairesse *et al.* [15], the phase of the high-order harmonics is related to two characteristic times: the time when the high-order harmonics is emitted (emission time t_e), and that when the electron recombines with the parent ion (recombination time t_r). In this section we review these relations.

First we discuss the emission time t_e of the high-order harmonics. Let us consider the high-order harmonics

$$E_{\mathrm{HH}}(t) = \sum_n A^{(2n+1)} \cos\left[(2n+1)\omega_0 t - \phi_{\mathrm{HH}}^{(2n+1)}\right], \tag{1}$$

generated by the driving field

$$E^{\mathrm{driving}}(t) = E_0^{\mathrm{driving}} \cos\left[\omega_0 t\right]. \tag{2}$$

In the work by Mairesse *et al.* [15] it is shown that the time t_e when the harmonic with frequency $\sim 2n\omega_0$ is emitted is related to the phase differences between adjacent harmonic orders $\Delta\phi_{\mathrm{HH}}^{(2n)} \equiv \phi_{\mathrm{HH}}^{(2n+1)} - \phi_{\mathrm{HH}}^{(2n-1)}$ by

$$t_e \simeq \frac{\Delta\phi_{\mathrm{HH}}^{(2n)}}{2\omega_0}. \tag{3}$$

In Ref. [15] the relation (3) is derived with the approximation $d\phi/d\omega \simeq \Delta\phi_{\mathrm{HH}}^{(2n)}/(2\omega_0)$. The relation (3) can also be derived without this approximation as follows: Equation (1) can be rewritten as

$$\begin{aligned} E_{\mathrm{HH}}(t) &= \sum_n (A'^{(2n)} + A'^{(2n+2)}) \cos\left[(2n+1)\omega_0 t - \phi_{\mathrm{HH}}^{(2n+1)}\right] \\ &= \sum_n A'^{(2n)} \left\{ \cos\left[(2n+1)\omega_0 t - \phi_{\mathrm{HH}}^{(2n+1)}\right] + \cos\left[(2n-1)\omega_0 t - \phi_{\mathrm{HH}}^{(2n-1)}\right]\right\} \\ &= \sum_n 2A'^{(2n)} \cos\left[2n\omega_0 t - \frac{\phi_{\mathrm{HH}}^{(2n+1)} + \phi_{\mathrm{HH}}^{(2n-1)}}{2}\right] \cos\left\{\omega_0\left[t - \frac{\Delta\phi_{\mathrm{HH}}^{(2n)}}{2\omega_0}\right]\right\}, \end{aligned} \tag{4}$$

where $A'^{(2n)} + A'^{(2n+2)} = A^{(2n+1)}$ with $A'^{(0)} = 0$. Equation (4) shows that the superposition of odd-order harmonics [Eq. (1)] is equivalent to the superposition of trains of wave packets with carrier frequency $2n\omega_0$ whose maxima of the envelope lag behind those of the driving field [Eq. (2)] by $t_e \simeq \Delta\phi_{\mathrm{HH}}^{(2n)}/2\omega_0$.

Next, we consider the relation between the recombination time t_r of the electron and the phase of the high-order harmonics. Under the strong-field approximation with the saddle-point approximation [17–19], the electron which ionizes at time t_i and recombines with the parent ion at t_r generates a pulse of harmonics with the spectrum of $F(\omega)e^{+i\omega t_r}$, where

$$\begin{aligned} F(\omega) \equiv \omega^2 \frac{i2\pi}{\sqrt{\det S_{\mathrm{st}}(t_i;t_r)}} \left(\frac{\pi}{i\tau/2+\epsilon}\right)^{3/2} e^{-iS_{\mathrm{st}}(t_i;t_r)} \\ \times \left[\boldsymbol{E}(t_i)\cdot\boldsymbol{d}(\boldsymbol{p}_{\mathrm{st}}(t_i;t_r)+\boldsymbol{A}(t_i))\right] d^*(\boldsymbol{p}_{\mathrm{st}}(t_i;t_r)+\boldsymbol{A}(t_r)). \end{aligned} \tag{5}$$

Here, $\tau \equiv t_r - t_i$ is the flight time of the electron, ϵ is a positive small value to remove the unphysical singularity, $\boldsymbol{E}(t)$ is the electric field of the driving pulse, $\boldsymbol{A}(t) \equiv -\int_0^t dt' \boldsymbol{E}(t')$, $S_{\mathrm{st}}(t_i;t_r) \equiv \int_{t_i}^{t_r}\{[\boldsymbol{p}_{\mathrm{st}} + \boldsymbol{A}(t'')]^2/2 + I_P\}dt''$, and $\boldsymbol{p}_{\mathrm{st}}(t_i;t_r) \equiv -\frac{1}{\tau}\int_{t_i}^{t_r} \boldsymbol{A}(t'')dt''$. The ionization time t_i and the recombination time t_r are the solutions of the saddle-point equations

$$\frac{[\boldsymbol{p}_{\mathrm{st}}(t_i;t_r)+\boldsymbol{A}(t_r)]^2}{2} + I_P - \omega = 0, \tag{6}$$

$$\frac{[\boldsymbol{p}_{\mathrm{st}}(t_i;t_r)+\boldsymbol{A}(t_i)]^2}{2} + I_P = 0. \tag{7}$$

The transition dipole moment $\boldsymbol{d}$ is defined by

$$\boldsymbol{d}(\boldsymbol{p}) \equiv (2\pi)^{-3/2} \int_{-\infty}^{+\infty} d^3\boldsymbol{x}\, e^{-i\boldsymbol{p}\cdot\boldsymbol{x}} \boldsymbol{x}\, \psi_0(\boldsymbol{x}). \tag{8}$$

For the periodicity of the driving field, the ionization and recombination will occur periodically. We assume that by satisfying an appropriate phase matching condition [20] only the short trajectory is selected per one half cycle of the driving field. When $T \equiv 2\pi/\omega_0$ denotes the cycle of the driving field, the harmonic fields are generated with their polarity reversed alternately at every one half cycle $T/2$ (Fig. 1), and consequently the spectrum of the harmonic field becomes

$$\begin{aligned} \tilde{E}_{\mathrm{HH}}(\omega) &\propto \sum_n (-1)^n F(\omega) e^{+i\omega t_r} e^{+in\omega T/2} \\ &= 2\omega_0 F(\omega) e^{+i\omega t_r} \sum_{n=-\infty}^{+\infty} \delta\left[\omega - (2n+1)\omega_0\right]. \end{aligned} \tag{9}$$

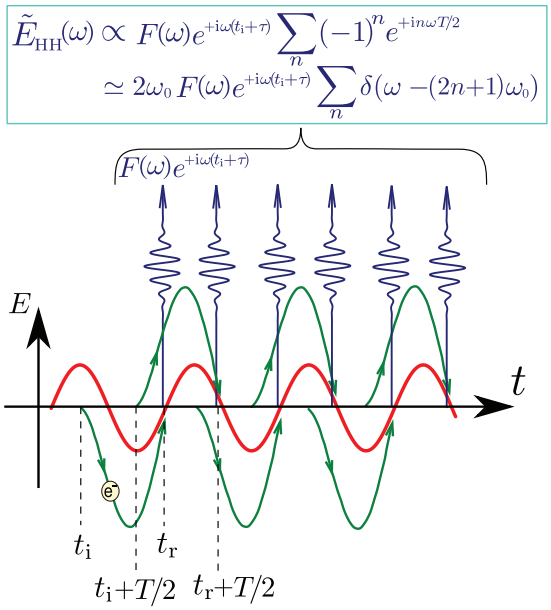

FIG. 1. (Color online) The periodic structure of the high-order harmonics. The harmonic fields are generated with their polarity reversed alternately at every one half cycle $T/2$.

From this we find that the $(2n+1)$th harmonic has a phase $\phi_{\rm HH}^{(2n+1)}$ which is the sum of the phase of $F[(2n+1)\omega_0]$, which we write as $\phi_F^{(2n+1)}$, and the term $(2n+1)\omega_0 t_r$:

$$\phi_{\rm HH}^{(2n+1)} = \phi_F^{(2n+1)} + (2n+1)\omega_0 t_r. \tag{10}$$

Therefore, the recombination time t_r is related to the phase difference $\Delta\phi_{\rm HH}^{(2n)}$ as

$$t_r = \frac{\Delta\phi_{\rm HH}^{(2n)}}{2\omega_0} - \frac{\phi_F^{(2n+1)} - \phi_F^{(2n-1)}}{2\omega_0}. \tag{11}$$

If the phase of the $F(\omega)$ is constant and $\phi_F^{(2n+1)} = \phi_F^{(2n-1)}$, the right-hand side of Eq. (11) is equal to that of Eq. (3), and the emission time of harmonics t_e is equal to the recombination time t_r. However, this is not true when $\phi_F^{(2n+1)}$ depends on the harmonic order $(2n+1)$.

To summarize, the phase difference $\Delta\phi_{\rm HH}^{(2n)}$ is not necessarily proportional to the recombination time t_r [Eq. (11)], in contrast to the emission time t_e [Eq. (3)]. Equation (11) shows that the emission time t_e lags $(\phi_F^{(2n+1)} - \phi_F^{(2n-1)})/2\omega_0$ behind the recombination time t_r, so the harmonic order dependence of $\phi_F^{(2n+1)}$ must be taken into consideration when the relation between $\Delta\phi_{\rm HH}^{(2n)}$ and t_r is discussed.

B. Detection technique of the phase difference by using two-photon ionization

As a method to observe the phase differences of high-order harmonics, we employ a technique called RABBIT (reconstruction of attosecond beating by interference of two-photon transitions) [10,15,21–26]. This method relies on the observation of the intensity variation of photoelectrons produced by two-photon ionization with the high-order harmonics to be measured and the fundamental near-infrared pulse for probing (hereafter called "probe pulse"). Considering that the photon energy of harmonics is odd multiple of the photon energy ω_0 of the driving field, the kinetic energies of the photoelectrons produced by $(2n-1)$th harmonics is $(2n-1)\omega_0 - I_{\rm P}$, where n is an integer and $I_{\rm P}$ is the ionization potential of the target atom. When the probe pulse is irradiated together with the high-order harmonics, the two-color two-photon ionization process with one high-order-harmonic photon and one photon in the probe pulse produces additional sidebands in between single-photon ionization signals. To the two-photon signal [$(2n)$th sideband] between the signals from the $(2n-1)$th and $(2n+1)$th harmonics, two processes can contribute: (1) absorption of one photon of the $(2n-1)$th harmonic and one photon of the probe pulse, and (2) absorption of one photon of the $(2n+1)$th harmonic and stimulated emission of one photon of the probe pulse. These two processes interfere with each other and consequently the intensity of the $(2n)$th sideband varies as a function of the delay Δt between high-order harmonics and the probe pulse. As shown below, the phase differences between adjacent harmonics are evaluated by analyzing the Δt dependence of the photoelectron signals thus produced.

Let us consider that the rare gas as a target is irradiated with the generated high-order harmonics and the probe pulse at the point to which the optical path length from the harmonic generation point is z as shown in Fig. 2. We write the electric fields of the $(2n\pm1)$th harmonics and the probe pulse at the detection point as

$$E_{\rm X}^{(2n\pm1)}(t) = \mathcal{A}_{\rm X}^{(2n\pm1)} e^{i\Phi_{\rm HH}^{(2n\pm1)}} e^{-i(2n\pm1)\omega_0 t} + \text{c.c.}, \tag{12}$$

$$E_{\rm I}(t) = \mathcal{A}_{\rm I} e^{i\Phi_{\rm probe}} e^{-i\omega_0 t} + \text{c.c.}, \tag{13}$$

respectively, where $\mathcal{A}_{\rm X}$, $\mathcal{A}_{\rm I}$, $\Phi_{\rm HH}^{(2n\pm1)}$, and $\Phi_{\rm probe}$ are real numbers. Within the second-order time-dependent perturbation

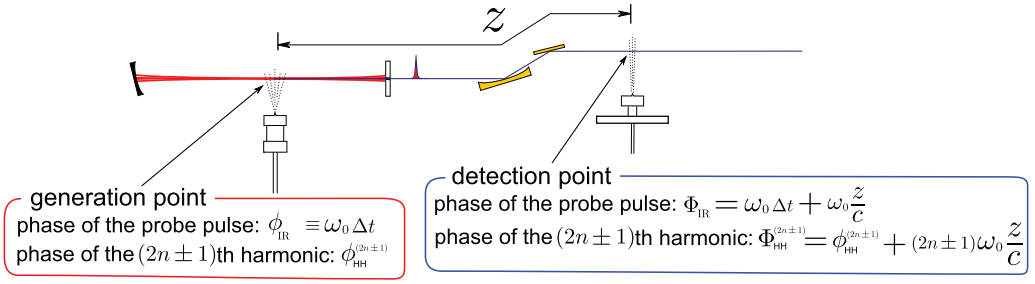

FIG. 2. (Color online) The relation between the phases at the generation point and that at the detection point.

theory, the intensity of the $(2n)$th sideband S_{2n} is calculated as

$$S_{2n} = \mathcal{A}_{\mathrm{I}}^2 \mathcal{A}_{\mathrm{X}}^{(2n-1)^2} A_{+}^{(2n+1)} + \mathcal{A}_{\mathrm{I}}^2 \mathcal{A}_{\mathrm{X}}^{(2n+1)^2} A_{-}^{(2n-1)} + \mathcal{A}_{\mathrm{I}}{}^2 \mathcal{A}_{\mathrm{X}}^{(2n-1)} \mathcal{A}_{\mathrm{X}}^{(2n+1)} A_{\mathrm{atom}}^{(2n)} \times \cos\left(2\Phi_{\mathrm{probe}} + \Phi_{\mathrm{HH}}^{(2n-1)} - \Phi_{\mathrm{HH}}^{(2n+1)} + \Delta\phi_{\mathrm{atom}}^{(2n)}\right). \quad (14)$$

Here, $A_{\pm}^{(2n\pm1)}$, $A_{\mathrm{atom}}^{(2n)}$, and $\Delta\phi_{\mathrm{atom}}^{(2n)}$ are constants representing the amplitudes and phase of the transition dipole, which are defined as

$$A_{\pm}^{(2n\pm1)} = \sum_{i,f} \left|\tilde{M}_{(f,i,\pm)}^{(2n)}\right|^2, \quad (15)$$

$$A_{\mathrm{atom}}^{(2n)} = 2\left|\sum_{i,f} \tilde{M}_{(f,i,+)}^{(2n)} \left(\tilde{M}_{(f,i,-)}^{(2n)}\right)^*\right|, \quad (16)$$

$$\Delta\phi_{\mathrm{atom}}^{(2n)} = \arg\left(\sum_{i,f} \tilde{M}_{(f,i,+)}^{(2n)} \left(\tilde{M}_{(f,i,-)}^{(2n)}\right)^*\right), \quad (17)$$

where

$$\tilde{M}_{(f,i,\pm)}^{(2n)} \equiv M_{(f,i)}^{(2n\mp1)} + M_{(f,i)}^{(\pm1)}, \quad (18)$$

$$M_{(f,i)}^{(q)} \equiv \sum\!\!\!\!\!\!\int_m \frac{\langle f|z|m\rangle \langle m|z|i\rangle}{E_i^0 + q\omega_0 - E_m^0}. \quad (19)$$

In Eq. (19), the intermediate state $|m\rangle$ runs all of the eigenstate of the atom, and $\sum\!\!\!\!\!\!\int_m$ means sum if $|m\rangle$ is a bound state and integral if $|m\rangle$ is a continuum state. The term $\Delta\phi_{\mathrm{atom}}^{(2n)}$ in Eq. (14), called an "atomic phase," can be calculated by using the method reported in Ref. [27]. When we neglect the dispersion of the medium gases for high-order-harmonic generation and the optical path difference between high-order harmonics and the probe pulse, the phase of the $(2n \pm 1)$th harmonics $\Phi_{\mathrm{HH}}^{(2n\pm1)}$ and that of the probe pulse Φ_{probe} at the detection point are related to the phase of the $(2n \pm 1)$th harmonics $\phi_{\mathrm{HH}}^{(2n\pm1)}$ and that of the probe pulse ϕ_{probe} at the generation point as

$$\Phi_{\mathrm{HH}}^{(2n\pm1)} = \phi_{\mathrm{HH}}^{(2n\pm1)} + \frac{(2n \pm 1)\omega_0}{c} z, \quad (20)$$

$$\Phi_{\mathrm{probe}} = \phi_{\mathrm{probe}} + \frac{\omega_0}{c} z, \quad (21)$$

respectively. The phase of the probe pulse ϕ_{probe} at the generation point can be controlled by changing the delay of the probe pulse Δt:

$$\phi_{\mathrm{probe}} = \omega_0 \Delta t. \quad (22)$$

Substituting Eqs. (20)–(22) into Eq. (14), we obtain

$$S_{2n} = \mathcal{A}_{\mathrm{I}}^2 \mathcal{A}_{\mathrm{X}}^{(2n-1)^2} A_{+}^{(2n+1)} + \mathcal{A}_{\mathrm{I}}^2 \mathcal{A}_{\mathrm{X}}^{(2n+1)^2} A_{-}^{(2n-1)} + \mathcal{A}_{\mathrm{I}}{}^2 \mathcal{A}_{\mathrm{X}}^{(2n-1)} \mathcal{A}_{\mathrm{X}}^{(2n+1)} A_{\mathrm{atom}}^{(2n)} \times \cos\left[2\omega_0 \Delta t - \Delta\phi_{\mathrm{HH}}^{(2n)} + \Delta\phi_{\mathrm{atom}}^{(2n)}\right]. \quad (23)$$

Thus we can directly get $\Delta\phi_{\mathrm{HH}}^{(2n)} \equiv \phi_{\mathrm{HH}}^{(2n+1)} - \phi_{\mathrm{HH}}^{(2n-1)}$ by observing the dependence of the sideband intensity S_{2n} on Δt.

III. EXPERIMENTAL SETUP

Figure 3 shows the schematic diagram of our experimental setup. An output from a Ti:sapphire based chirped-pulse amplification system (FEMTOLASERS Produktions GmbH, FEMTOPOWER PRO V CEP) is spatially divided by a drilled mirror 1 into an outer annular beam and an inner small beam. The outer beam (8 mm diam. with a hole of 4 mm diam.) is used as a "driving pulse" for high-order-harmonic generation. The inner beam is further spatially confined by an iris to 2 mm diam., and used as a probe pulse of the RABBIT method. The pulse energies of the driving and the probe pulses are ~0.2 and ~0.02 mJ, respectively. The peak intensity of the driving pulse is estimated to be $> 10^{14}$ W/cm^2 at the focus, and that of the probe pulse is to be on the order of 10^{12} W/cm^2 because at the focus the beam radius of the probe pulse is larger than that of the driving pulse by a factor of 2. The delay Δt between the driving and the probe pulses is controlled by a closed-loop piezoelectric positioning stage with resolution of 10 nm [SIGMA KOKI Co. Ltd., SFS-H60X(CL)]. The two pulses are combined collinearly by another drilled mirror 2, and are then introduced into the vacuum chamber and focused by a concave mirror into a supersonic atomic or molecular gas jet, in which high-order harmonics are generated. The gas jet for generating high-order harmonics is introduced through a pulsed valve (Parker-Hannifin, 009-1670-900) with the orifice diameter of 0.1 mm. The position of the focus is set before the gas jet to select the contribution from the short trajectories [20]. An aperture is located ~400 mm after the focus, which blocks the outer annular beam, while the generated XUV harmonics and the inner probe pulse pass through the aperture [28]. The harmonics and the probe pulses are refocused into the supersonic gas jet of Ar by a gold-coated toroidal mirror to ionize the Ar atom by an XUV photon or by two photons of one XUV photon and one IR photon. The kinetic energy and the angular distribution of the produced photoelectrons are measured by using the velocity-map imaging technique [29]: The produced photoelectrons are accelerated toward the two-dimensional detector (Hamamatsu Photonics, F2226-24PF132) by the static electric field formed by the three electrodes, which is adjusted so that electrons with the same initial momenta are imaged onto almost the same position of the screen, irrespective of their initial positions. The light blobs on the phosphor screen are focused by a 50-mm-focal-length lens on a charge-coupled device (CCD) camera (Basler, avA2300-30km). The image is transferred

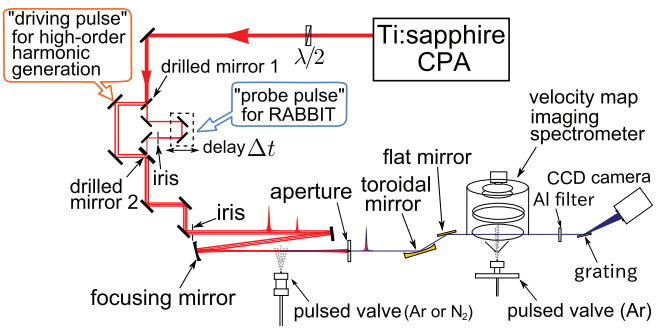

FIG. 3. (Color online) Schematic diagram of the experimental setup. See text for the details.

to a personal computer through a frame grabber (Euresys, GrabLink Base). The three-dimensional velocity distribution is reconstructed by the BASEX method [30]. In addition to the photoelectron measurement, we also observe the intensity spectra of high-order harmonics with an XUV spectrometer with a CCD camera. With the spectrometer we detected the harmonics up to 43rd generated both in N_2 and in Ar, from which we estimate the intensity of the driving pulse as $\sim 2.7 \times 10^{14}$ W/cm^2.

IV. RESULTS

The left panel of Fig. 4 shows the reconstructed image of photoelectron velocity distribution produced by single-photon ionization of Ar with high-order harmonics generated in N_2 molecules. The concentric rings reflect single-photon ionization by the respective orders of harmonics. The innermost ring corresponds to the 11th harmonics and the ring corresponding to the 19th harmonics is observed in our setup. In the right panel of Fig. 4, the reconstructed image of photoelectrons is shown when the probe pulse is introduced together with the XUV pulses. Additional rings in between single-photon ionization signals are attributed to the signals of two-color two-photon ionization.

We observe the velocity distribution at each delay Δt and obtain the intensities of the sidebands as a function of Δt. From Eq. (23) it is expected that the sideband intensities S_{2n} show the $\cos(2\omega_0\Delta t + \phi)$-shape variation. In practice, however, the $\cos(2\omega_0\Delta t + \phi)$-shape variation in the sideband is subject to the $\cos(\omega_0\Delta t)$-like modulation of the harmonic amplitude $\mathcal{A}_{\rm X}^{(2n\pm1)}$. This modulation comes from the interference of the driving pulse and the probe pulse focused into the Ar and N_2 gas jet to generate high-order harmonics. Although the intensity of the probe pulses ($\sim 10^{12}$ W/cm^2) is lower by two orders of magnitude than that of the driving pulse ($\sim 10^{14}$ W/cm^2), the magnitude of the electric field is lower by only one order and their interference causes a modulation in harmonic intensities due to the high nonlinearity of the high-order-harmonic generation process. In Refs. [21,22], the effect of the modulation in harmonic intensities is removed simply by dividing the sideband intensity at each Δt by the total photoelectron signal at this delay. Here we normalize S_{2n} by using a physically meaningful method based on Eq. (23), which is derived by considering the production process of photoelectrons. When both sides of Eq. (23) are divided by

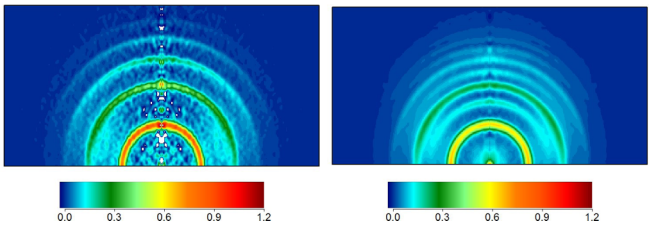

FIG. 4. (Color online) Velocity distributions of photoelectrons produced by single-photon ionization of Ar with high-order harmonics from N_2 (left panel) and by two-color photoionization with high-order harmonics from N_2 and the probe pulses (right panel).

$\mathcal{A}_{\rm X}^{(2n-1)}\mathcal{A}_{\rm X}^{(2n+1)}$ [the factor before the $\cos(2\omega_0\Delta t + \phi)$ term], we get

$$\begin{aligned}\tilde{S}_{2n} &\equiv S_{2n}\big/\big(\mathcal{A}_{\rm X}^{(2n-1)}\mathcal{A}_{\rm X}^{(2n+1)}\big)\\ &= \mathcal{A}_{\rm I}^2\left[\frac{\mathcal{A}_{\rm X}^{(2n-1)}}{\mathcal{A}_{\rm X}^{(2n+1)}}A_+^{(2n+1)} + \frac{\mathcal{A}_{\rm X}^{(2n+1)}}{\mathcal{A}_{\rm X}^{(2n-1)}}A_-^{(2n-1)}\right.\\ &\quad\left. + A_{\rm atom}^{(2n)}\cos\left(2\omega_0\Delta t - \Delta\phi_{\rm HH}^{(2n)} + \Delta\phi_{\rm atom}^{(2n)}\right)\right]. \quad (24)\end{aligned}$$

This normalized sideband intensity $\tilde{S}_{2n}$ is robust against the modulation in harmonic intensities because before the $\cos(2\omega_0\Delta t + \phi)$ term there are no factors about the harmonic intensities. In addition, the effect of the harmonic intensity modulation on the two terms $(\mathcal{A}_{\rm X}^{(2n-1)}/\mathcal{A}_{\rm X}^{(2n+1)})A_+^{(2n+1)}$ and $(\mathcal{A}_{\rm X}^{(2n+1)}/\mathcal{A}_{\rm X}^{(2n-1)})A_-^{(2n-1)}$ is opposite and cancel each other out. The normalizing factor $\mathcal{A}_{\rm X}^{(2n-1)}\mathcal{A}_{\rm X}^{(2n+1)}$ is estimated from the signals of single-photon ionization: The probability of single-photon ionization is proportional to the intensity of the light, and thus to the square of the amplitude of the electric field. Therefore, the normalizing factor $\mathcal{A}_{\rm X}^{(2n-1)}\mathcal{A}_{\rm X}^{(2n+1)}$ is proportional to the square root of the product of the single-photon ionization signals by $(2n-1)$th and $(2n+1)$th harmonics.

The normalized intensities $\tilde{S}_{2n}$'s of the 12th–18th sidebands for Ar and for N_2 are shown as a function of Δt in Figs. 5(a) and 5(b), respectively. By comparing Eqs. (2) and (22), we define the origin of the horizontal axis $\Delta t = 0$ as the point where the electric field of the driving pulse and that of the probe pulse are in phase. Here we determine $\Delta t = 0$ by choosing the delay so that the driving and the probe pulses interfere constructively in the same way as used in Refs. [15,23]. The $\cos(2\omega_0\Delta t + \phi)$-shape modulations clearly appear in Fig. 5, but there still remain small components with the frequency ω_0. Equation (24) suggests that the remaining components come from the change in the probe intensity $\mathcal{A}_{\rm I}^2$ as a function of Δt. Reference [22] pointed out the possibility that some part of the driving pulse is scattered by the gaseous medium and is focused on the gas for detection without being blocked by the aperture (see Fig. 3). Another plausible reason is the coupling between the driving pulse and the probe pulse through the change of the nonlinear refractive index induced by the two pulses [31, §11.6]. We assume that the probe intensity $\mathcal{A}_{\rm I}^2$ varies like $\cos(\omega_0\Delta t + \eta)$ plus a constant, and fit the normalized sideband by a function

$$A[1 + B\,\cos(\omega_0\Delta t + \eta)][1 + C\,\cos(2\omega_0\Delta t + \phi)], \quad (25)$$

with A, B, C, η, and ϕ the fitting parameters.

The phase difference $\Delta\phi_{\rm HH}^{(2n)}$ is obtained from the fitting parameter ϕ by subtracting the atomic phase $\Delta\phi_{\rm atom}^{(2n)}$ [see Eq. (24)]. The resuts for Ar and N_2 are shown in Fig. 6 by squares and triangles, respectively. We calculate $\Delta\phi_{\rm atom}^{(2n)}$ within the second-order perturbation theory and the single-active-electron approximation with the one-electron potential proposed in Refs. [27,32] by using the method of Toma and Muller [27]. The calculated $\Delta\phi_{\rm atom}^{(2n)}$'s are shown in the inset of Fig. 6. We determine $\Delta\phi_{\rm HH}^{(2n)}$ within the range of $0 < \Delta\phi_{\rm HH}^{(2n)} \leqslant 2\pi$. The error bars represent those associated

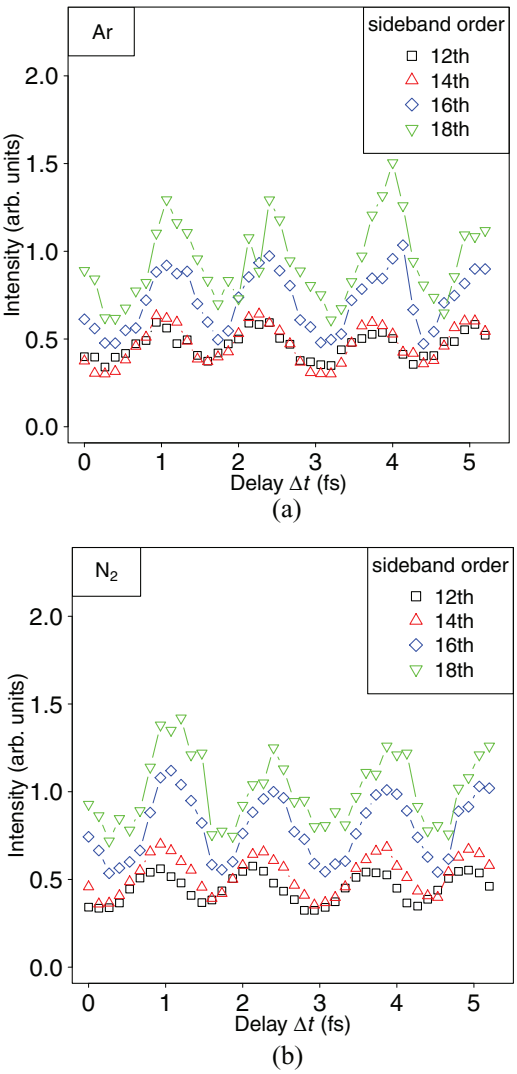

FIG. 5. (Color online) The intensities of 12th–18th sidebands for Ar (a) and for N_2 (b) as a function of Δt. To remove the undesired modulation in harmonic intensities, the $(2n)$th sideband intensity is normalized by the square root of the product of the single-photon ionization signals from $(2n-1)$th and $(2n+1)$th harmonics.

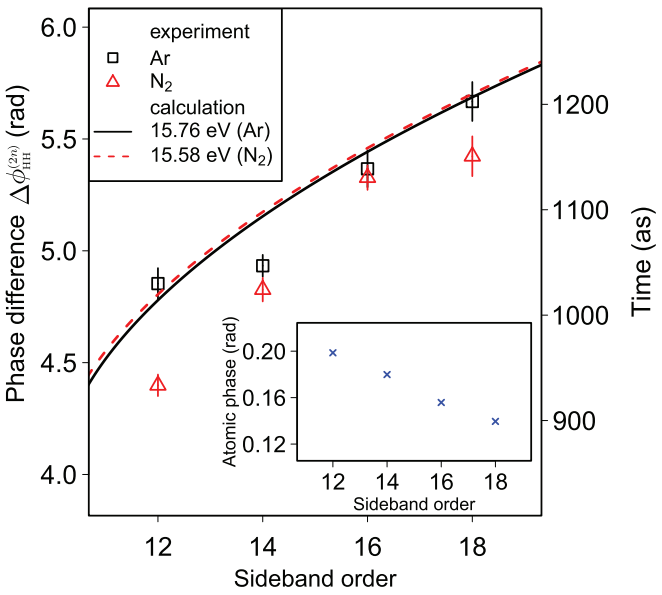

FIG. 6. (Color online) Points with error bars: $\Delta\phi_{\rm HH}^{(2n)}$ for Ar (squares) and N_2 (triangles), obtained by fitting the modulation of sideband intensities shown in Fig. 5. The emission time t_e of each harmonic calculated by Eq. (3) is read by the right vertical axis. Curves: the recombination time t_r calculated by using the saddle-point method within the strong-field approximation [15,18], at the laser intensity of 2.7×10^{14} W/cm^2. Inset: the atomic phase $\Delta\phi_{\rm atom}^{(2n)}$ calculated by the second-order perturbation theory [27] with a one-electron potential given in Refs. [27,32].

with the least-squares fitting. To check the validity of our analysis, we also compute the discrete Fourier transform of the data in Fig. 5 and compare the phases of the component at $2\omega_0$ with those obtained by the fitting. We confirm that all the results obtained by Fourier analysis fall in the fitting results well within the fitting errors. As described in Sec. II A, the times t_e when the harmonics are emitted are related to the phase differences as $t_e \simeq \Delta\phi_{\rm HH}^{(2n)}/2\omega_0$ [Eq. (3)]. Shown by the right vertical axis in Fig. 6 are t_e's corresponding to the observed phase differences.

V. DISCUSSIONS

The phase differences $\Delta\phi_{\rm HH}^{(2n)}$ monotonically increase as a function of the sideband order. As shown by Mairesse *et al.* [15], this feature is considered to come from the tendency that the recombination time t_r of the short trajectory becomes larger for higher photon energy. We show in Fig. 6 the recombination time t_r calculated by using the saddle-point method within the strong-field approximation [17–19] (see Sec. II A). The calculation is done for short trajectories at the laser intensity of 2.7×10^{14} W/cm^2 and for $I_P = 15.76$ eV (solid line) and 15.58 eV (dashed line), which corresponds to Ar and N_2, respectively [33]. In Fig. 6 the recombination times t_r are related to the phase differences $\Delta\phi_{\rm HH}^{(2n)}$ by Eq. (11) with the assumption that the phase of the $F(\omega)$ [Eq. (5)] is independent of the photon energy ω and thus $t_r \simeq t_e \simeq \Delta\phi_{\rm HH}^{(2n)}/2\omega_0$. Though the results of the model calculation reproduce the increase of the phase differences as a function of the harmonic order, we find that this calculation cannot reproduce the following point found in our observations: From the calculated result it is expected that the phase differences $\Delta\phi_{\rm HH}^{(2n)}$ for Ar and those for N_2 are almost the same at each sideband order. However, at the 12th sideband, nearest to the ionization thresholds, a remarkable difference appears between the experimental result of Ar and that of N_2. In the case of Ar, $\Delta\phi_{\rm HH}^{(12)}$ is almost the same as $\Delta\phi_{\rm HH}^{(14)}$, which deviates from the increasing tendency of t_r's predicted by the model calculation. This characteristic behavior is also found in the results by Aseyev *et al.* [23]. On the other hand, for N_2, the value of $\Delta\phi_{\rm HH}^{(2n)}$ increases monotonically over the entire sideband orders observed and $\Delta\phi_{\rm HH}^{(12)}$ is considerably lower than $\Delta\phi_{\rm HH}^{(14)}$. In the following we discuss the reason for the difference in $\Delta\phi_{\rm HH}^{(12)}$ between Ar and N_2.

First we check up on the possibility that the difference between Ar and N_2 is caused by the change in the experimental condition. A possible effect to be considered is the difference

in the medium dispersion, the importance of which is pointed out by Dinu *et al.* [22]. To take the dispersion into account, we consider a simple model in which Eqs. (20) and (21) are replaced by

$$\Phi_{\rm HH}^{(2n\pm1)} = \phi_{\rm HH}^{(2n\pm1)} + \frac{(2n\pm1)\omega_0}{c}(z-\Delta z) + n\left[(2n\pm1)\omega_0\right]\frac{(2n\pm1)\omega_0}{c}\Delta z, \quad (26)$$

$$\Phi_{\rm probe} = \phi_{\rm probe} + \frac{\omega_0}{c}(z-\Delta z) + n(\omega_0)\frac{\omega_0}{c}\Delta z, \quad (27)$$

where $n(\omega)$ is the refractive index of the medium at the angular frequency ω and Δz is the effective interaction length of the medium. Then, the argument of the cosine term in the intensity modulation of the sideband [Eq. (24)] is changed into

$$\begin{aligned} &2\omega_0\Delta t - \Delta\phi_{\rm HH}^{(2n)} + \Delta\phi_{\rm atom}^{(2n)} \\ &\quad\rightarrow 2\omega_0\Delta t - \Delta\phi_{\rm HH}^{(2n)} + \Delta\phi_{\rm atom}^{(2n)} \\ &\qquad - \{(2n+1)n[(2n+1)\omega_0] - 2n(\omega_0) \\ &\qquad - (2n-1)n\left[(2n-1)\omega_0\right]\}\frac{\omega_0\Delta z}{c}. \end{aligned} \quad (28)$$

To estimate the degree of the dispersion effect on the phase differences, let us assume that the gas produces one free electron per atom, as assumed in Ref. [22]. Then, the dielectric constant is given by $\epsilon(\omega)/\epsilon_0 = 1-\omega_{\rm P}^2/\omega^2$, where $\omega_{\rm P}$ is the plasma frequency defined by $\omega_{\rm P}^2 = Ne^2/(\epsilon_0 m)$ [34, §7.5]. The refractive index becomes

$$n(\omega) \simeq \sqrt{\epsilon(\omega)/\epsilon_0} = \sqrt{1-\frac{\omega_{\rm P}{}^2}{\omega^2}} \simeq 1 - NA\frac{1}{\omega^2}, \quad (29)$$

where $A = e^2/(2\epsilon_0 m)$ is a constant. Then, the correction term in Eq. (28) is estimated as follows:

$$\begin{aligned} &\{(2n+1)n\left[(2n+1)\omega_0\right] - 2n(\omega_0) \\ &\qquad - (2n-1)n[(2n-1)\omega_0]\}\frac{\omega_0\Delta z}{c} \\ &\simeq N\frac{(2n)^2-3}{(2n)^2-1}\frac{A}{c\omega_0}\Delta z. \end{aligned} \quad (30)$$

This shows that the $\Delta\phi_{\rm HH}^{(2n)}$ has a correction term which linearly depends on the plasma density N. Figure 7 shows the correction term $N\frac{(2n)^2-3}{(2n)^2-1}\frac{A}{c\omega_0}\Delta z$ given by Eq. (30) as a function of the sideband order. Based on our experimental condition, we choose the parameters as $N = 1\times10^{18}$ cm^{-3} and $\Delta z = 0.1$ mm. Although the correction brought by the dispersion effect is monotonically increased as a function of the sideband order, its contribution to the phase difference is very small ($<2\times10^{-3}$ rad) over the observed sideband order.

Another factor which can affect the experimental results is the optical path difference between high-order harmonics and the probe pulse due to the slight change of the alignment. When the optical path length from the generation point to the detection point is z for high-order harmonics, and that for the probe pulse is larger than z by δz, Eq. (21) is replaced by

$$\Phi_{\rm probe} = \omega_0\Delta t + \frac{\omega_0}{c}(z+\delta z). \quad (31)$$

In this case, the argument of the cosine term in the intensity modulation of the sideband [Eq. (24)] is changed into

$$\begin{aligned} &2\omega_0\Delta t - \Delta\phi_{\rm HH}^{(2n)} + \Delta\phi_{\rm atom}^{(2n)} \\ &\quad\rightarrow 2\omega_0\Delta t - \Delta\phi_{\rm HH}^{(2n)} + \Delta\phi_{\rm atom}^{(2n)} + 2\frac{\omega_0}{c}\delta z. \end{aligned} \quad (32)$$

Since the magnitude of the correction $(2\omega_0/c)\delta z$ does not depend on the sideband order, the misalignment of the probe pulse simply leads to the overall shift in the phase differences.

The change in the intensity of the driving pulse can also vary the phase differences because it changes the recombination time $t_{\rm r}$ of the electron. Figure 8 compares the results of the same model calculations as those used in Fig. 6 done at three laser intensities of 2.7×10^{14} W/cm^2 (solid curve), 2.0×10^{14} W/cm^2 (dashed curve), and 1.5×10^{14} W/cm^2 (dot-dashed curve). The ionization potential $I_{\rm P}$ is 15.76 eV. As the intensity of the driving pulse decreases, the curve of the

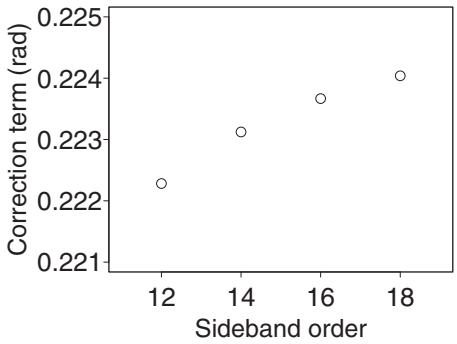

FIG. 7. The correction term $N\frac{(2n)^2-3}{(2n)^2-1}\frac{A}{c\omega_0}\Delta z$ given by Eq. (30) with $N = 1\times10^{18}$ cm^{-3} and $\Delta z = 0.1$ mm.

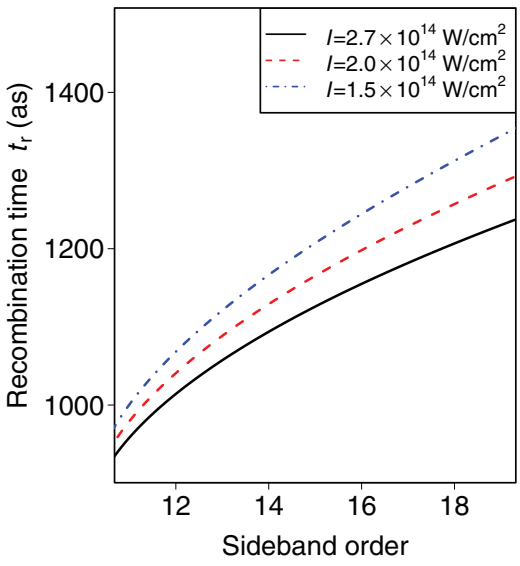

FIG. 8. (Color online) The results of the model calculation at three laser intensities of 2.7×10^{14} W/cm^2 (solid curve), 2.0×10^{14} W/cm^2 (dashed curve), and 1.5×10^{14} W/cm^2 (dot-dashed curve). The ionization potential $I_{\rm P}$ is set at 15.76 eV.

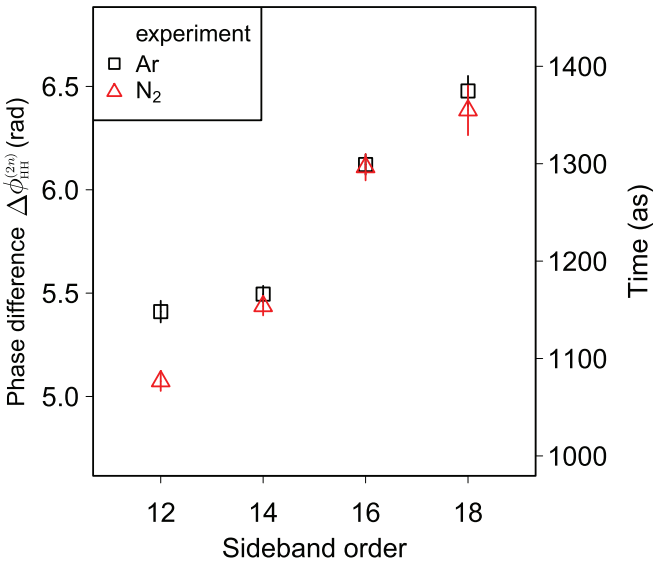

FIG. 9. (Color online) The experimental results observed four months after the observation leading to the results shown in Fig. 6.

recombination time t_r shifts upward. The shape of the curve, however, is almost unchanged.

All of the three effects discussed above can cause the overall shift of $\Delta\phi_{\rm HH}^{(2n)}$'s, but the amount of the shift is little or not dependent on the sideband order. In fact, when we measured the $\Delta\phi_{\rm HH}^{(2n)}$'s of the high-order harmonics generated in Ar and N_2 four months after the observation leading to the results shown in Fig. 6, the shift of the absolute values of $\Delta\phi_{\rm HH}^{(2n)}$'s are observed (Fig. 9), which is considered to be due to the slight changes in the density of the medium, in the optical path difference between high-order harmonics and the probe pulse, and in the driving pulse intensity. However, the behavior of $\Delta\phi_{\rm HH}^{(2n)}$ as a function of the sideband order is very similar to that of Fig. 6, and the difference in $\Delta\phi_{\rm HH}^{(12)}$ between Ar and N_2 is clearly reproduced. Therefore, we conclude the difference in $\Delta\phi_{\rm HH}^{(12)}$ between Ar and N_2 comes from the intrinsic property of the medium in which high-order harmonics are generated. Since the ionization potentials I_P of Ar and N_2 are 15.76 and 15.58 eV, respectively, and the photon energy of the driving pulses is $\sim$1.55 eV, the ionization threshold of Ar and N_2 corresponds to $\simeq$10th harmonics and the 12th sideband is very near the ionization threshold. As discussed in Sec. I, several phenomena are reported that cannot be explained by the strong-field approximation [12–14]. In the following, we investigate the plausible causes of the anomaly in $\Delta\phi_{\rm HH}^{(12)}$ by considering the corrections of the strong-field approximation.

To investigate the physical origin of the difference between Ar and N_2, we focus on Eq. (11) which relates the recombination time t_r of the electron to the phase difference $\Delta\phi_{\rm HH}^{(2n)}$. Equation (11) can be rewritten as

$$\Delta\phi_{\rm HH}^{(2n)} = 2\omega_0 t_r + \left(\phi_F^{(2n+1)} - \phi_F^{(2n-1)}\right). \tag{33}$$

This equation suggests the following two possibilities: (1) the recombination time t_r is different between Ar and N_2, and (2) the second term of the right-hand side $(\phi_F^{(2n+1)} - \phi_F^{(2n-1)})$ in Eq. (33) is different between Ar and N_2.

First we consider the recombination time t_r. In the model calculation of t_r presented in Fig. 6 the shape of the potential created by the parent ion is neglected, but it is natural to think that the difference in the potential shape between Ar and N_2 will influence t_r. To investigate the effect of the potential of the parent ion, we calculate t_r with the classical trajectory Monte Carlo method [14,35]. We consider one-dimensional classical trajectories of a single active electron driven by the laser field in the soft-core potential

$$V(x) = -Z_e/\sqrt{x^2+\alpha^2}, \tag{34}$$

and calculate the time when an electron with a positive energy (corresponding to the ionization) returns to the origin $x = 0$ (corresponding to the recombination). As the initial distribution of the position x and momentum p we use the truncated Wigner distribution [35]: that is, we first calculate the quantum ground state, and based on this ground state we obtain the (x,p) distribution which can be allowed in the classical mechanics. Figure 10(b) shows the calculated recombination times for three different potentials [Fig. 10(a)] with the same ionization energy $I_P = 15.58$ eV but different parameters Z_e and α in Eq. (34). The intensity of the driving pulse is set at 2.7×10^{14} W/cm^2. By the right vertical axis we show the phase differences $\Delta\phi_{\rm HH}^{(2n)}$ calculated by Eq. (33) assuming $\phi_F^{(2n+1)} - \phi_F^{(2n-1)} = 0$. Depending on the parameters of the soft-core potential, the slope slightly changes over all the harmonic energy range rather than only around the 12th sideband. Moreover, the change in the t_r is small compared to that resulting from the experimentally observed difference in $\Delta\phi_{\rm HH}^{(12)}$ between Ar and N_2. Thus the effect of the potential shape on the recombination time of the returning electron does not seem to be a major cause for the observed difference in $\Delta\phi_{\rm HH}^{(12)}$. If, on the other hand, at the near-threshold region the multiphoton ionization dominates in the first step of the high-order-harmonic generation process as pointed out in Ref. [14], the difference in the structure of the excited states between Ar and N_2 largely affects the ionization process, which will change the recombination time t_r of the returning electron.

Next we consider the term $(\phi_F^{(2n+1)} - \phi_F^{(2n-1)})$ in Eq. (33). We recall that $\phi_F^{(2n+1)}$ is defined in Sec. II A as the phase of $F[(2n+1)\omega_0]$, and $F(\omega)$ is the spectrum of the harmonics defined in Eq. (5). Equation (5) shows that $F(\omega)$ is proportional to the recombination dipole $d^*(\boldsymbol{p}_{\rm st}(t_i;t_r) + \boldsymbol{A}(t_r))$. In Sec. II A, under the strong-field approximation, the continuum state in the transition dipole moment $\boldsymbol{d}$ is expressed by a plane wave $e^{-i\boldsymbol{p}\cdot\boldsymbol{x}}$ [Eq. (8)] without considering the effects of the Coulomb potential. However, it is well known in the scattering theory that the Coulomb potential can influence a charged particle in a faraway place due to its slow falloff [36, §14]. Moreover, in the recombination process the electron must return to the parent ion and the effect of the Coulomb interaction is inevitable. Therefore it is natural to include the effect of the potential in the recombination dipole moment. In Fig. 11 we show by the solid line the phase of the photorecombination transition dipole moment for Ar calculated by reference to Ref. [16], with the one-electron potential presented in Refs. [27,32]. The phase changes rapidly toward the ionization threshold due

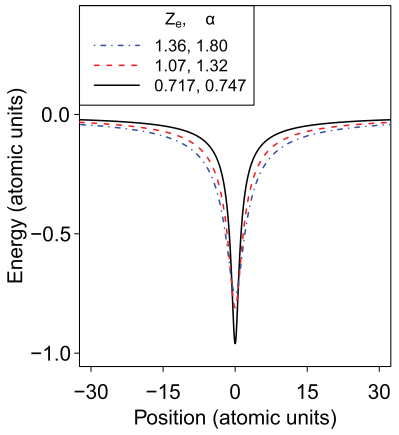

(a)

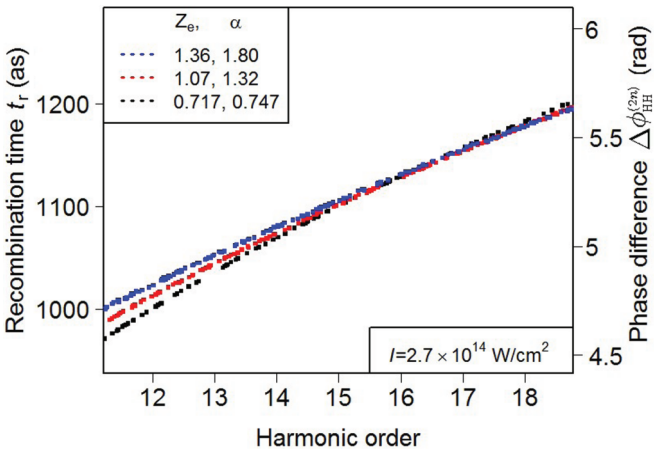

(b)

FIG. 10. (Color online) (a) Three different one-dimensional soft-core potentials [Eq. (34)] used in the classical trajectory Monte Carlo calculations. (b) The recombination times calculated with the classical trajectory Monte Carlo method in three different soft-core potentials. The parameters for the soft-core potentials are given in the legends. The intensity of the driving pulse is 2.7×10^{14} W/cm^2.

to the Coulomb potential made by the parent ion. This rapid phase change can provide a large $(\phi_F^{(2n+1)} - \phi_F^{(2n-1)})$ in Eq. (33) around the photon energy of the 12th sideband order, which makes the $\Delta\phi_{HH}^{(12)}$ deviate from the value predicted from the t_r calculated with the simple assumption of $\phi_F^{(2n+1)} - \phi_F^{(2n-1)} = 0$. We also show by the broken line in Fig. 11 the phase of the dipole moment calculated by using the returning electron wave packet uninfluenced by the potential, i.e., the plane-wave approximation. Its large difference from the result including the effect of the potential means that the potential made by the parent ion actually can play a crucial role in the harmonic phase around the near-threshold energy range. The difference in the shape of the potential between Ar and N_2 will make $(\phi_F^{(13)} - \phi_F^{(11)})$ different from each other and accordingly cause the difference in $\Delta\phi_{HH}^{(12)}$ between them. Note that the phase of $F(\omega)$ can also be affected by the shape of the valence orbital with which the electron recombines [25]. For example, in the high-order-harmonic spectrum of Ar the harmonic phase jumps around 40–50 eV [16] associated

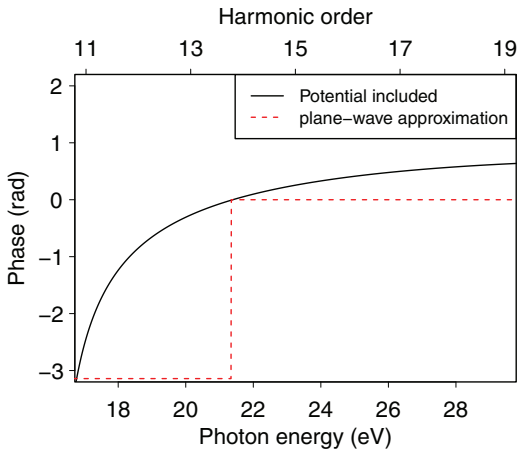

FIG. 11. (Color online) Calculated phase of the photorecombination transition dipole moment for Ar with the one-electron potential presented in Refs. [27,32] (solid line) and with the plane-wave approximation (broken line).

with the Cooper minimum [37,38]. However, the position of the harmonic phase jump resulting from the structure of the valence orbital is also affected by the potential of the parent ion. The importance of the potential on the position of the phase jump can be seen in Fig. 11: The phase jump associated with the Cooper minimum, which should appear around 40–50 eV as stated above, occurs unphysically at ∼21 eV when calculated with the Coulomb potential neglected [16]. Since the effect of the Coulomb potential of the parent ion on the harmonic phase is so complicated, further investigations will be needed for quantitative discussions about the phase difference we found in the present experiment.

VI. CONCLUSION AND OUTLOOK

We observed the phase differences $\Delta\phi_{HH}^{(2n)}$ of high-order harmonics generated from Ar atoms and N_2 molecules. Although the behavior of $\Delta\phi_{HH}^{(2n)}$ above the 14th sideband order is well described by the strong-field approximation, we found that $\Delta\phi_{HH}^{(12)}$ is significantly different between Ar and N_2. After carefully considering some possible reasons which may cause the difference in $\Delta\phi_{HH}^{(12)}$ between them, we conclude that this difference comes from the particularity of high-order harmonics near the ionization potential I_P, or more specifically, mainly from the difference in the shape of the Coulomb potential made by the parent ion, though a deeper understanding of the underlying physics of near-threshold high-order harmonics is still required. Therefore the present study demonstrates that the observation of the phase differences of near-threshold high-order harmonics can become a new probe of the shape of the potentials or the structure of the excited states. This new probe will surely add further to the advantages of imaging of atomic and molecular orbitals based on high-order-harmonic generation [39].

We point out two future directions along the present study. One is to observe the phase differences with a longer-wavelength driving pulse. In the present experiment we used the output from a femtosecond Ti:sapphire laser with the center wavelength of ∼800 nm as a driving pulse. Then

high-order harmonics are generated at the energy interval of ∼3.1 eV, which is rather sparse for detailed investigations of the high-order-harmonic generation process around the near-threshold region. In fact, the deviation from the model calculation appears only at the 12th sideband $\Delta\phi_{\mathrm{HH}}^{(12)}$ in the present observation. When a longer-wavelength driving pulse is employed, the spectra of high-order harmonics become denser and provide us with richer information about the high-order-harmonic generation process. The other is to observe the phase differences of near-threshold high-order harmonics generated in well aligned or oriented molecules, which will serve to reveal the effect of the anisotropy of the potential created by the parent molecular ions.

ACKNOWLEDGMENTS

We are grateful to Kei Nakagawa and Yo Iida for their assistance in the present experiment and for their insightful discussions. We express our deep gratitude to Dr. Jiro Itatani for valuable advice and comments. This work was supported by Grant-in-Aid for Specially Promoted Research, Grant No. 21000003, from MEXT and the Photon Frontier Network Program of MEXT. K.K. is grateful for the financial support from the Global COE Program "Physical Sciences Frontier," MEXT, Japan. K.K. and Y.S. are grateful for the financial support from Grant-in-Aid for JSPS Fellows, Grants No. 12J10272 and No. 13J10603, respectively.

[1] F. Krausz and M. Ivanov, Rev. Mod. Phys. **81**, 163 (2009).
[2] M. Nisoli and G. Sansone, Prog. Quantum Electron. **33**, 17 (2009).
[3] P. Salières, A. Maquet, S. Haessler, J. Caillat, and R. Taïeb, Rep. Prog. Phys. **75**, 062401 (2012).
[4] P. B. Corkum, Phys. Rev. Lett. **71**, 1994 (1993).
[5] M. Lewenstein, P. Balcou, M. Y. Ivanov, A. L'Huillier, and P. B. Corkum, Phys. Rev. A **49**, 2117 (1994).
[6] J. Itatani, J. Levesque, D. Zeidler, H. Niikura, H. Pépin, J. C. Kieffer, P. B. Corkum, and D. M. Villeneuve, Nature (London) **432**, 867 (2004).
[7] T. Kanai, S. Minemoto, and H. Sakai, Nature (London) **435**, 470 (2005).
[8] S. Baker, J. S. Robinson, C. A. Haworth, H. Teng, R. A. Smith, C. C. Chirilă, M. Lein, J. W. G. Tisch, and J. P. Marangos, Science **312**, 424 (2006).
[9] O. Smirnova, Y. Mairesse, S. Patchkovskii, N. Dudovich, D. Villeneuve, P. Corkum, and M. Y. Ivanov, Nature (London) **460**, 972 (2009).
[10] S. Haessler, J. Caillat, W. Boutu, C. Giovanetti-Teixeira, T. Ruchon, T. Auguste, Z. Diveki, P. Breger, A. Maquet, B. Carré, R. Taïeb, and P. Salières, Nat. Phys. **6**, 200 (2010).
[11] H. J. Wörner, J. B. Bertrand, D. V. Kartashov, P. B. Corkum, and D. M. Villeneuve, Nature (London) **466**, 604 (2010).
[12] N. H. Burnett, C. Kan, and P. B. Corkum, Phys. Rev. A **51**, R3418 (1995).
[13] K. Miyazaki and H. Takada, Phys. Rev. A **52**, 3007 (1995).
[14] H. Soifer, P. Botheron, D. Shafir, A. Diner, O. Raz, B. D. Bruner, Y. Mairesse, B. Pons, and N. Dudovich, Phys. Rev. Lett. **105**, 143904 (2010).
[15] Y. Mairesse, A. de Bohan, L. J. Frasinski, H. Merdji, L. C. Dinu, P. Monchicourt, P. Breger, M. Kovacev, R. Taieb, B. Carre, H. G. Muller, P. Agostini, and P. Salieres, Science **302**, 1540 (2003).
[16] A.-T. Le, R. R. Lucchese, S. Tonzani, T. Morishita, and C. D. Lin, Phys. Rev. A **80**, 013401 (2009).
[17] M. Lewenstein, P. Salières, and A. L'Huillier, Phys. Rev. A **52**, 4747 (1995).
[18] P. Salières, B. Carre, L. Le Deroff, F. Grasbon, G. G. Paulus, H. Walther, R. Kopold, W. Becker, D. B. Milosevic, A. Sanpera, and M. Lewenstein, Science **292**, 902 (2001).
[19] G. Sansone, C. Vozzi, S. Stagira, and M. Nisoli, Phys. Rev. A **70**, 013411 (2004).
[20] P. Antoine, A. L'Huillier, and M. Lewenstein, Phys. Rev. Lett. **77**, 1234 (1996).
[21] P. M. Paul, E. S. Toma, P. Breger, G. Mullot, F. Auge, P. Balcou, H. G. Muller, and P. Agostini, Science **292**, 1689 (2001).
[22] L. C. Dinu, H. G. Muller, S. Kazamias, G. Mullot, F. Augé, P. Balcou, P. M. Paul, M. Kovačev, P. Breger, and P. Agostini, Phys. Rev. Lett. **91**, 063901 (2003).
[23] S. A. Aseyev, Y. Ni, L. J. Frasinski, H. G. Muller, and M. J. J. Vrakking, Phys. Rev. Lett. **91**, 223902 (2003).
[24] R. López-Martens, K. Varjú, P. Johnsson, J. Mauritsson, Y. Mairesse, P. Salières, M. B. Gaarde, K. J. Schafer, A. Persson, S. Svanberg, C.-G. Wahlström, and A. L'Huillier, Phys. Rev. Lett. **94**, 033001 (2005).
[25] W. Boutu, S. Haessler, H. Merdji, P. Breger, G. Waters, M. Stankiewicz, L. J. Frasinski, R. Taieb, J. Caillat, A. Maquet, P. Monchicourt, B. Carre, and P. Salieres, Nat. Phys. **4**, 545 (2008).
[26] Z. Diveki, R. Guichard, J. Caillat, A. Camper, S. Haessler, T. Auguste, T. Ruchon, B. Carré, A. Maquet, R. Taïeb, and P. Salières, Chem. Phys. **414**, 121 (2013).
[27] E. S. Toma and H. G. Muller, J. Phys. B: At. Mol. Opt. Phys. **35**, 3435 (2002).
[28] J. Peatross, J. L. Chaloupka, and D. D. Meyerhofer, Opt. Lett. **19**, 942 (1994).
[29] A. T. J. B. Eppink and D. H. Parker, Rev. Sci. Instrum. **68**, 3477 (1997).
[30] V. Dribinski, A. Ossadtchi, V. A. Mandelshtam, and H. Reisler, Rev. Sci. Instrum. **73**, 2634 (2002).
[31] R. W. Boyd, *Nonlinear Optics*, 3rd ed. (Academic, New York, 2008).
[32] H. G. Muller, Phys. Rev. A **60**, 1341 (1999).
[33] NIST computational chemistry comparison and benchmark database, NIST Standard Reference Database Number 101, Release 16a, August 2013, edited by Russell D. Johnson III, http://cccbdb.nist.gov/
[34] J. D. Jackson, *Classical Electrodynamics*, 3rd ed. (Wiley, New York, 1998).
[35] P. Botheron and B. Pons, Phys. Rev. A **80**, 023402 (2009).
[36] J. R. Taylor, *Scattering Theory: The Quantum Theory of Nonrelativistic Collisions* (Dover, New York, 2006).
[37] S. Minemoto, T. Umegaki, Y. Oguchi, T. Morishita, A.-T. Le, S. Watanabe, and H. Sakai, Phys. Rev. A **78**, 061402 (2008).
[38] A.-T. Le, T. Morishita, and C. D. Lin, Phys. Rev. A **78**, 023814 (2008).
[39] M. Lein, J. Phys. B: At. Mol. Opt. Phys. **40**, R135 (2007).